NANO · MICRO small
www.small-journal.com

A 3.2 V Binary Layered Oxide Cathode for Potassium-Ion Batteries

*Pawan Kumar Jha, Shubham Kumar Parate, Krishnakanth Sada, Kazuki Yoshii, Titus Masese, Pavan Nukala, Gopalakrishnan Sai Gautam, Valérie Pralong, Maximilian Fichtner, and Prabeer Barpanda**

Potassium-ion batteries (KIBs) can offer high energy density, cyclability, and operational safety while being economical due to the natural abundance of potassium. Utilizing graphite as an anode, suitable cathodes can realize full cells. Searching for potential cathodes, this work introduces P3-type $K_{0.5}Ni_{1/3}Mn_{2/3}O_2$ layered oxide as a potential candidate synthesized by a simple solid-state method. The material works as a 3.2 V cathode combining Ni redox at high voltage and Mn redox at low voltage and exhibits highly reversible K^+ ion (de)insertion at ambient and elevated (40–50 °C) temperatures. First-principles calculations suggest the ground state in-plane Mn–Ni ordering in the MO_2 sheets is strongly correlated to the K-content in the framework, leading to an interwoven and alternative row ordering of Ni–Mn in $K_{0.5}Ni_{1/3}Mn_{2/3}O_2$. Postmortem and electrochemical titration reveal the occurrence of a solid solution mechanism during K^+ (de)insertion. The findings suggest that the Ni addition can effectively tune the electronic and structural properties of the cathode, leading to improved electrochemical performance. This work provides new insights in the quest to develop potential low-cost Co-free KIB cathodes for practical applications in stationary energy storage.

1. Introduction

Lithium-ion batteries (LIBs) are ubiquitous in the 21st century thanks to their high energy density, long cycle life, and reliable performance.[1] However, the ever-growing energy storage demand and the limited availability of lithium resources call for the development of alternative battery technologies.[1b] It has led to the development of various post-lithium-ion batteries with operational similarity, comparable energy density, safety, and low cost, which is crucial to ensure a sustainable energy future.[2] Potassium-ion batteries (KIBs) are one such alternative energy storage technology. Potassium is more abundant than lithium and has a lower redox potential, which allows for higher voltage and energy density. In comparison to Na, K offers several unique advantages: i) its lower redox potential (vs standard hydrogen electrode) typically leads to higher voltages, ii) it can

P. K. Jha, K. Sada, P. Barpanda
Faraday Materials Laboratory (FaMaL)
Materials Research Centre
Indian Institute of Science
Bangalore 560012, India
E-mail: prabeer@iisc.ac.in

S. K. Parate, P. Nukala
Center for Nano Science and Engineering
Indian Institute of Science
Bangalore 560012, India

K. Yoshii, T. Masese
Research Institute of Electrochemical Energy
Department of Energy and Environment (RIECEN)
National Institute of Advanced Industrial Science and Technology (AIST)
1-8-31 Midorigaoka, Ikeda, Osaka 563–8577, Japan

The ORCID identification number(s) for the author(s) of this article can be found under https://doi.org/10.1002/smll.202402204

DOI: 10.1002/smll.202402204

G. Sai Gautam
Department of Materials Engineering
Indian Institute of Science
Bangalore 560012, India

V. Pralong
ENSICAEN
UNICAEN
CNRS
CRISMAT
Normandie University
Caen 14000, France

V. Pralong
Réseau sur le Stockage Electrochimique de l'Énergie (RS2E)
Amiens France

M. Fichtner, P. Barpanda
Electrochemical Energy Storage
Helmholtz Institute Ulm (HIU)
89081 Ulm, Germany

M. Fichtner, P. Barpanda
Institute of Nanotechnology
Karlsruhe Institute of Technology (KIT)
76021 Karlsruhe, Germany

reversibly intercalate into graphite anode, and iii) its low Stokes radius (weaker interaction with solvent and anions) enables faster K^+ mobility in the electrolyte.[3] Additionally, lower negative electrode potential vis-à-vis Li/Li^+ (−0.1 V vs Li) in carbonate ester solvents such as propylene carbonate (PC) and ethylene/diethyl carbonate (EC: DEC) yields the widest potential window (≈4.6 V compared to 4.5 and 4.2 V for Li and Na respectively) for KIBs without K plating on the anode side.[2a,3a,b] Despite numerous advances, the practical realization of KIBs is dependent on the development of suitable electrolytes and robust positive insertion hosts (or cathodes) capable of reversible K^+ (de)intercalation.

Owing to the larger ionic size of K^+ (1.38 Å) [vis-à-vis Na^+ (1.02 Å) and Li^+ (0.76 Å),[4] it is challenging to discover cathode materials for KIBs as compared to LIBs or Na-ion batteries. Numerous classes of materials, including well-known layered transition-metal oxides, have been evaluated as cathodes for KIBs. Layered oxide materials offer 2D K^+ migration pathways along with high energy density.[5] Based on the ionic size, the stable coordination environments of K^+ as well as transition metal can be quite different from the Li- and Na-based systems.[6] Also, most of these oxides stabilize in K-deficient stoichiometry with K^+ ions having prismatic coordination.[5b,7] The preference of (trigonal) prismatic coordination over the octahedral stacking sequence of anion packing can be explained through the size and electrostatics, as well as from the "Rouxel" and "cationic potential" phase maps, as has been shown in our previous study.[6b,8] Out of the P2- and P3-prismatic stacking frameworks, P3-type layered oxides are suitable to develop KIB cathodes owing to i) simple and scalable synthesis, ii) efficient K^+ migration in 2D open frameworks,[5] and iii) superior structural integrity over P2- and O3-type oxides during cycling.

P3-type layered oxides have been explored before synergizing experimental and computational tools. In particular, the Mn-based oxides have drawn much attention because of their low cost, environmental friendliness, and variable oxidation states (2+ to 7+) offering tunable redox potential.[9] Kim et al. reported reversible K^+ (de)insertion in a P3-type $K_{0.5}MnO_2$ host, where progressive K^+ (de)insertion involves several complex phase transformations leading to structural disintegration at low K content.[10] Moreover, stacking faults and other structural defects result in rapid capacity fading even with a lower upper voltage cut-off. Building on the fundamental understanding gained from Na-based systems, partial replacement of Mn metal with other transition metals (Ti, Fe, Co, Ni, Cu, and Zn) or non-redox active elements (Mg, Ca, and Al) improves both cyclability and average redox potential owing to the suppression of strong Jahn–Teller distortion associated with high-spin Mn^{3+} ($3d^4$) species and K^+/vacancy ordering.[10,11] In this quest, partial substitution of Ni increases the average oxidation state of Mn, which in turn results in high electronic conductivity as well as the facile migration of K^+ ion apart from the increase in capacity due to $Ni^{2+}\leftrightarrow Ni^{4+}$ redox during K^+ (de)intercalation.[12]

In this work, we have designed a novel P3-type layered oxide $K_{0.5}Ni_{1/3}Mn_{2/3}O_2$ (referred to as KNM now onward) as a potential cathode with high reversible capacity both at ambient and high temperatures. Crystallizing in a P3-layered structure with $R3m$ symmetry, it exploits high electronic and ionic conductivity facilitated by Ni incorporation. We have investigated the structural, morphological, electronic, and electrochemical properties of KNM synergizing experimental measurements and density functional theory (DFT)[13] calculations. Our computations indicate that the K-content influences the ground state ordering in the lattice, specifically the Ni–Mn ordering in the transition metal layer, similar to the prior experimental observation in Na-based oxide insertion materials.[14] Importantly, we observe KNM to yield an average of 3.2 V (vs K/K^+) with high structural reversibility, superior rate capability, good cycle performance, and nearly 100% Coulombic efficiency even after 100 cycles across two different electrochemical potential cut offs. We find the electrochemical activity to be stable even at higher temperatures (≈40 °C and 50 °C). Our findings not only unearth a novel cathode composition for KIBs but also provide insights to develop economic and high energy density cathode materials for next-generation K-ion batteries targeting large-scale energy storage.

2. Results

2.1. Structural and Physical Characterizations

KNM layered oxide was synthesized using the conventional scalable (dry) solid-state route as well as the (wet) sol–gel route. The synthesis protocols are sketched as a schematic in Figure S1 (Supporting Information) of the electronic supplementary information (ESI). Both synthesis protocols led to the desired KNM product (Figure S2, Supporting Information). Rietveld analysis of the powder XRD pattern confirmed the product has a desired rhombohedral structure with $R3m$ (#160) symmetry consistent with the reported structure of $K_{0.48}Co_{0.6}Mn_{0.4}O_2$ (**Figure 1a**).[15] A negligible amount (≈2.28%) of NiO impurity was traced. The details of structure and lattice parameters are given in Table S1 (Supporting Information). KNM has a rhombohedral framework with an ABBCCA stacking of oxygen layers. The structure is built with alternating layers of K atoms and $(MO_2)_n$ sheets constituting edge-sharing MO_6 (M = Mn, Ni) octahedra. The K atoms assume a trigonal prismatic environment (Figure 1b). Geometrically, the oxygen ions of MO_6 octahedra in neighboring $(MO_2)_n$ sheets are directly above/below each other to create prismatic sites accommodating K^+ ions. The KO_6 trigonal prisms share one face with MO_6 octahedra and three edges with MO_6 octahedra of the opposite sheet (Figure 1a, inset). The final lattice parameters were calculated as: $a = b = 2.887$ (3) Å, $c = 20.665$ (15) Å, and volume (V) = 149.186 (4) $Å^3$. Additionally, the ICP-OES (Inductively Coupled Plasma – Optical Emission Spectrometry) derived elemental ratio K:Ni:Mn = 0.508:0.347:0.663 aligned closely with the nominal composition.

The local structure was further probed by Raman spectroscopy, which revealed two distinct Raman-active modes located at 472 cm^{-1} (E_g) and 620 cm^{-1} (A_{1g}) (Figure 1c). It is in good agreement with the factor group analysis of $R3m$ space group with a corresponding spectroscopic space group of D^5_{3d}.[16] They are related to M–O (M = Ni and Mn) stretching, where two oxygen atoms vibrate in the opposite direction along the c-axis, and O–M–O bending, where alternative vibrations occur in opposite directions parallel to K and Mn–Ni planes. The intensity of A_{1g} band

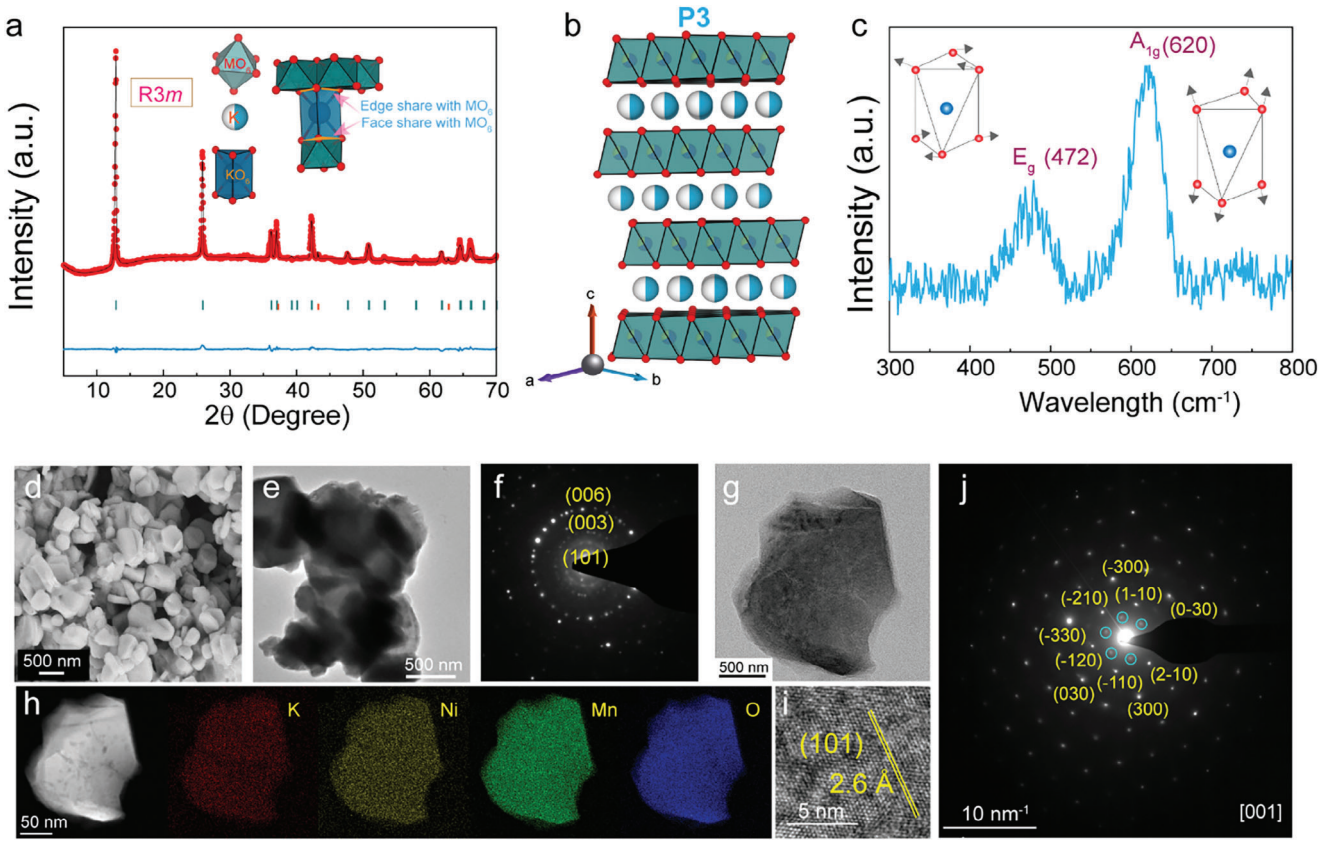

Figure 1. a) Rietveld refined powder XRD pattern ($\lambda = 1.5405$ Å) of P3-$K_{0.5}Ni_{1/3}Mn_{2/3}O_2$ material. The experimental data (red dots), calculated pattern (black line), difference curve (blue line), and Bragg diffraction positions (green ticks for the target P3 and orange ticks for the minor impurity NiO Phase) are shown ($\chi^2 = 8.16$). b) P3-type layered structure with 0.5 site occupancy of K^+ ions. c) Characteristic Raman spectrum of KNM showing the Raman active modes. Morphology of KNM as revealed by d) scanning electron microscopy (SEM) micrograph, e) bright field transmission electron microscopy (TEM) image, f) selected area electron diffraction (SAED) pattern, g, h) elemental mapping TEM-energy dispersive X-ray spectroscopy (TEM-EDS) confirming homogeneous distribution of K, Ni, Mn, and O elements, i) high-resolution TEM (HRTEM) image showing fringes representing (101) lattice planes. j) SAED pattern showing characteristic and superstructure spots in KNM (highlighted by blue circles).

is almost twice that of the E_g mode due to the higher oscillating strength associated with the A_{1g} mode.

The as-synthesized KNM was found to have a hexagonal platelet morphology with submicron particles in the size range of 0.3 to 0.6 µm (Figure 1d,e). Energy-dispersive X-ray spectroscopy (EDS, Figures S3 and S4, Supporting Information) and elemental mapping confirmed the presence and uniform distribution of constituent K, Ni, Mn, and O elements (Figure 1g,h). The high-resolution transmission electron microscopy (TEM) micrograph attested the crystallinity with the lattice fringes oriented along (101) direction having an interatomic planar spacing of ≈2.6 Å (Figure 1f,i). Selected area electron diffraction (SAED) pattern having the presence of concentric circles can be related to the hexagonal symmetry. Figure 1j shows the SAED pattern along the *c*-axis clearly revealing light spots (highlighted by blue circles) corresponding to the in-plane Ni-Mn superstructure ordering. Further, X-ray photoelectron spectroscopy (XPS) spectrum captured the signals of K 2*s*, K 2*p*, Ni 2*s*, Ni 2*p*, O 1*s*, Mn 2*s*, Mn 2*p* located at 975.39, 853.10, 772.48, 642.64, 530.43, 376.55 and 291.47 eV respectively, validating the presence and expected chemical states of the K^+, $Ni^{2+/3+}$ and $Mn^{3+/4+}$ in the pristine sample (Figure S5, Supporting Information).

2.2. Computational Studies

We performed DFT-based calculations, using the Hubbard *U* corrected strongly constrained and appropriately normed (or SCAN+*U*) exchange–correlation (XC) functional[17] to investigate the electronic structure of the KNM phase. The calculated lattice parameters and volume are close to the experimental observation except for the *c* lattice parameter, which deviates by 8–10%. As the interlayer spacing is higher, especially in K, van der Waals interactions may play a role during calculations. Hence, we have included van der Waals corrections with the SCAN+*U* functional (or SCAN+*U*+*vdw*) to quantify deviations with and without the corrections.[18] Additionally, we performed similar calculations with the Hubbard *U* corrected Perdew–Burke–Ernzerhof[17b] (or PBE+*U*) functional and the corresponding van der Waals corrected PBE+*U* (PBE+*U*+*vdw*) to provide a point of comparison to our SCAN-based calculations.[19] Table S2 (Supporting Information) compiles the lattice parameters and volumes, as calculated by PBE+*U* and SCAN+*U*, as well as with the corresponding van der Waals corrections, while **Figure 2a** plots the predicted *c* parameter by the four XC functionals. Notably, both PBE+*U* and SCAN+*U* calculations are in good agreement with

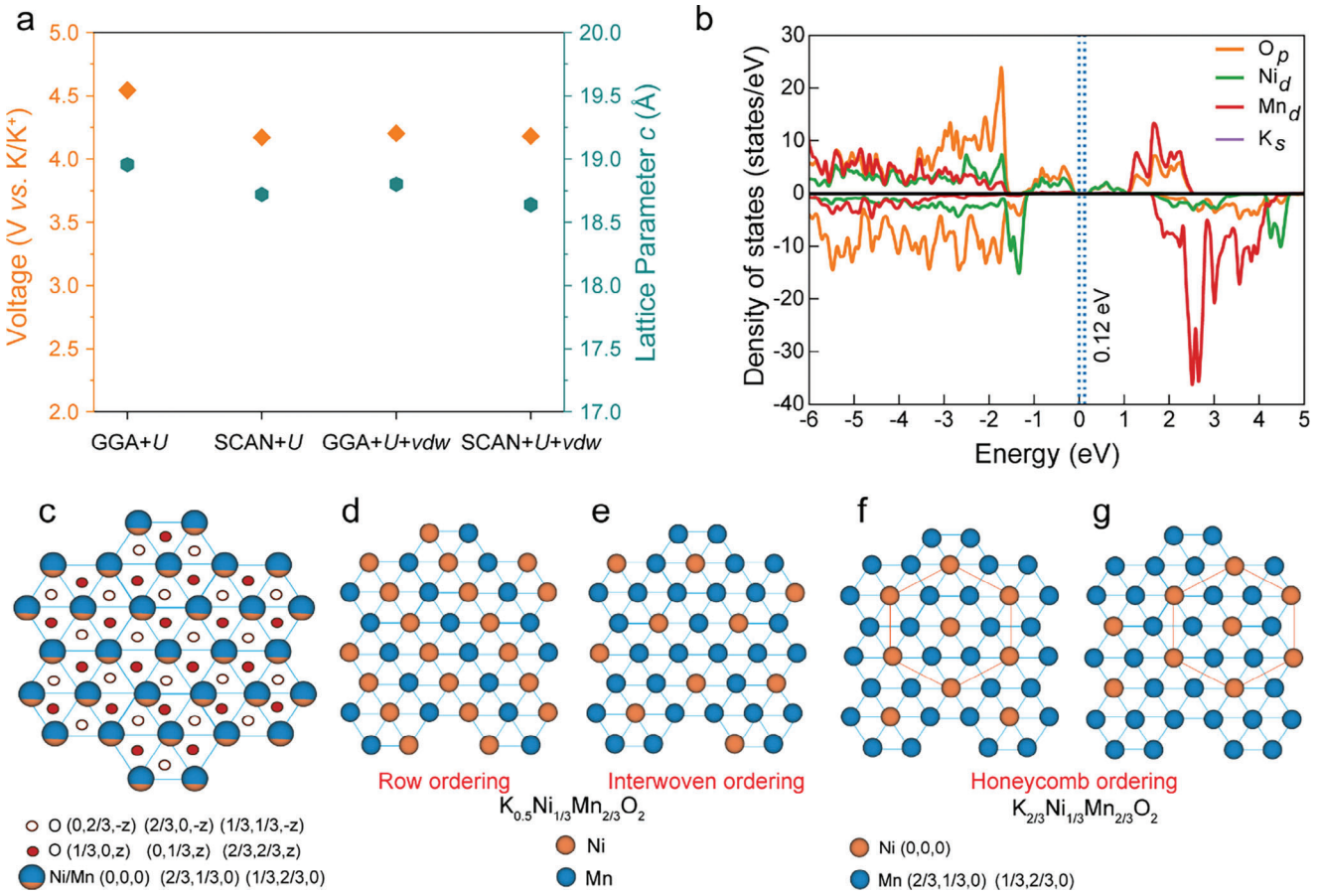

Figure 2. a) Average topotactic voltage (orange diamonds) and *c* lattice parameter (cyan hexagons) of P3-KNM system as predicted by the four XC functionals considered. b) The density of state (DOS) for P3-KNM, as calculated by SCAN+*U*. Orange, green, red, and purple curves correspond to the O 2*p*, Ni 3*d*, Mn 3*d*, and K 4*s* states, respectively. The dotted blue lines are valence and conduction band edges. The zero on the energy scale is set to the valence band maximum and the band gap is indicated by the text annotation. c) MO_2 sheet in P3-type layered oxides. Mixed color balls (orange and blue) represent the sites available for transition metal. Filled and open red circles represent the oxygen ion above and below the transition metal layer, respectively. d) In-plane row ordering at x = 0.5 in $K_xNi_{1/3}Mn_{2/3}O_2$ of Mn and Ni in the basal M layer, and e) in the adjacent M layer. f) $(\sqrt{3})a \times (\sqrt{3})a$ cation ordering (or honeycomb ordering) in MO_2 sheets at x = 2/3 in $K_xNi_{1/3}Mn_{2/3}O_2$ in the basal plane and g) non-basal layers in the supercell. The transition metals Ni and Mn are designated by orange and blue balls respectively.

experimental values, with PBE+*U* (SCAN+*U*) overestimating (underestimating) the lattice parameters (except *c*) by a maximum of 1.8% (0.3%) and are consistent with previous theoretical studies.[6a,20] We find the SCAN+*U* functional provides a quantitatively better agreement with experimental measurements than the PBE+*U* functional. Thus, we performed the electronic density of states (DOS) calculations with the SCAN+*U* functional and used SCAN+*U* on-site magnetic moment values for further analysis. Notably, all XC functionals underestimate the interlayer spacing or the *c* lattice parameter. Importantly, the inclusion of a van der Waals correction does not significantly affect the *c* lattice parameter with both PBE+*U* and SCAN+*U*.

As Ni and Mn exhibit different oxidation states in KNM, as quantified by their on-site magnetic moments (Table S3, Supporting Information), their electrostatic interaction with K^+ can influence the ordering in the MO_2 sheets. Similar experimental observations have been reported for several Li- and Na-based oxides.[14b] The crystallographic site A(0,0,0) for M in the P3 structure splits when there is a preferential occupancy between Mn and Ni. Importantly, our results suggest that the number of Ni and Mn in individual MO_2 layers are different. For instance, the basal layer consists of equal numbers of Mn and Ni (or "row ordering," see Figure 2d), while the adjacent layer has only ¼ of the available sites occupied by Ni ("interwoven ordering," Figure 2e).

Notably, all the KO_6 trigonal prisms share faces with the NiO_6 octahedra to minimize electrostatic interactions (Figure S6, Supporting Information). Indeed, our on-site magnetic moment data indicates that all Mn is in 4+ states, while Ni is equally distributed between 2+ and 3+ states. Moreover, NiO_6 octahedra share both the triangular faces that are oriented toward the K layers (i.e., "above" and "below") to further minimize electrostatic repulsions between K and M. Notably, the observed Ni–Mn ordering does not match with any previous reports, indicating the dependence of transition metal ordering on the K^+ content. To validate further that the in-plane M ordering depends on the K^+ concentration, we have calculated the ordering at x = 2/3 and x = 0 in P3-$K_xNi_{1/3}Mn_{2/3}O_2$ using the supercell of size

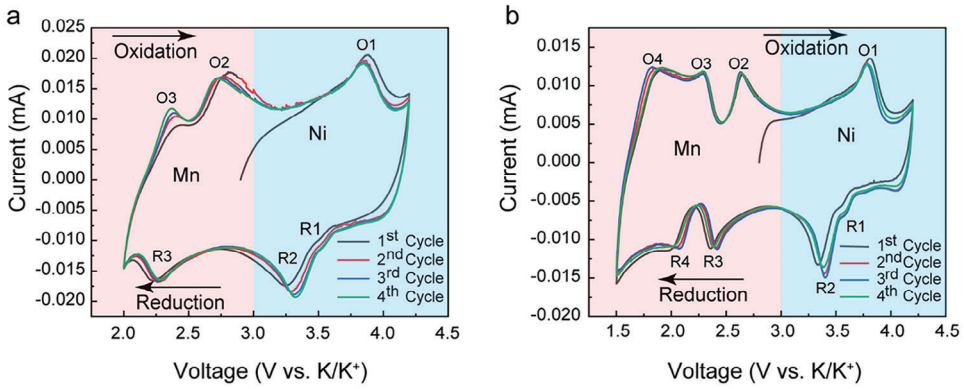

Figure 3. Cyclic voltammograms (CV) of KNM cathode in K-half cell at scan rates of 0.1 mV s^{-1} with two different voltage windows, a) 4.2–2 V, and b) 4.2–1.5 V.

$2\sqrt{3}a \times 2\sqrt{3}a$. Importantly, for x = 2/3 our most stable calculated structure shows the same Ni–Mn in-plane ordering, namely the "honeycomb ordering" of Figure 2f,g, as has been observed in P3-type $Na_{2/3}Ni_{1/3}Mn_{2/3}O_2$ via X-ray and neutron diffraction and in Li_2MnO_3.[14b] For the fully depotassiated state, we observed the basal (bottom) transition metal plane exclusively comprises Mn in the layer whereas the middle and top layers showcase an interwoven and a row ordering of Mn and Ni, respectively (Figure S7, Supporting Information).

Figure 2a presents the DFT calculated average topotactic voltages (in units of V *vs.* K/K^+) for the KNM host, across the $K_{0.5}Ni_{1/3}Mn_{2/3}O_2$-$Ni_{1/3}Mn_{2/3}O_2$ compositions. We observed that all XC functional calculations overestimate the average voltage by ≈1 V (Figure 4), similar to trends observed with SCAN+*U* in Li-containing layered transition metal oxides.[20a] The inclusion of van der Waals corrections does not affect the voltage with SCAN+*U*, however, we observed a little higher average voltage value in the case of GGA+*U*, similar to trends observed in Li-containing layered oxides.[20a] Further, to probe the redox mechanism, we analyzed the SCAN+*U* calculated on-site magnetic moments of Mn and Ni at potassiated (i.e., $K_{0.5}Ni_{1/3}Mn_{2/3}O_2$) and fully charged ($Ni_{1/3}Mn_{2/3}O_2$) states, which are listed in Table S3 (Supporting Information). Specifically, the potassiated ground state exhibits all Mn in a 4+ state, with half of Ni each in 2+ and 3+ states. Upon K removal, we observe a significant change in the onsite magnetic moment of Ni, whereas the Mn ions do not exhibit any change, suggesting the sole participation of Ni in the redox process and Mn^{4+} as a structural stabilizer. However, if excess K is inserted into the structure (i.e., beyond x = 0.5 in $K_xNi_{1/3}Mn_{2/3}O_2$), Mn may also participate in the redox process.

Figure 2b and Figure S8 (Supporting Information) display the SCAN+*U* calculated projected DOS (pDOS) of KNM and its fully charged analog, respectively. Our calculated pDOS indicates a semiconducting electronic structure for both the potassiated and charged compounds, with a predicted band gap of 0.12 and 1.19 eV, respectively. The substitution of Ni in place of Mn decreases the band gap (with a possible increase in electronic conductivity), as indicated by the predicted band gaps of 0.12 eV for KNM and 0.84 eV[6a] for P3-$K_{0.5}MnO_2$, which can be attributed to the filling of more *d* bands with Ni addition. The Ni-*d* and O-*p* states dominate both band edges in the potassiated state, and the conduction band edge in the charged state, while O-*p* states alone dominate the valence band edge in the charged state, suggesting a lack of participation of Mn-*d* states in the redox process. Thus, our pDOS data also suggests Ni redox being active on K removal from the host resulting in $Ni^{2+/3+}$ oxidation to Ni^{4+}, in sync with our calculated on-site magnetic moments (Table S3, Supporting Information) and experimental ex situ XPS and electrochemical measurements, as discussed in the subsequent sections.

2.3. Electrochemical Analyses

To gauge the electrochemical activity of the KNM composition, cyclic voltammetry (CV) was conducted at a scan rate of 0.1 mV s^{-1} across two different potential windows, namely, 4.2–1.5 and 4.2–2.0 V, as illustrated in **Figure 3**. The first oxidation peak at 3.84 V (O1) can be attributed to the Ni ($Ni^{2+/3+} \rightarrow Ni^{3+/4+}$) redox reaction, as it is the only predominant redox-active element, while Mn remains unchanged at higher potentials. In the subsequent oxidation cycles, a few more peaks appeared at lower voltages of 2.65 V (O2), 2.30 V (O3), and 1.88 V (O4) owing to the Mn redox reaction. During potassiation (reduction), four peaks were observed: 3.59 V (R1), 3.4 V (R2), 2.35 V (R3), and 2.05 V (R4), representing the reduction of both transition elements present in the system. The O1/R1, R2 arise due to $Ni^{4+}/Ni^{3+}/Ni^{2+}$ redox couple, while the O2, O3/R3, R4 stem from Mn^{4+}/Mn^{3+} redox couple. These redox curves neatly superimpose on subsequent cycling indicating excellent reversibility of the cathode. In addition, the broad nature of redox peaks indicates a topotactic K^+ (de)insertion reaction. The corresponding derivative capacity (dQ/dV) curves confirm the KNM host undergoes reversible phase transitions, with similar shapes for the anodic and cathodic profiles (Figure S9, Supporting Information). The curves in the high and low voltage regions are in accordance with the CV profiles observed for both the narrow (4.2–2 V) and wider (4.2–1.5 V) electrochemical potential windows. Furthermore, the electrochemical characteristics of the KNM host remain consistent even at high temperatures (Figure S10, Supporting Information).

Subsequently, the galvanostatic (dis)charge performance of KNM was tested in potassium half-cells at a scanning rate of 0.05C (C/20 or 6.22 mAg^{-1}) at room temperature. A 0.5 M

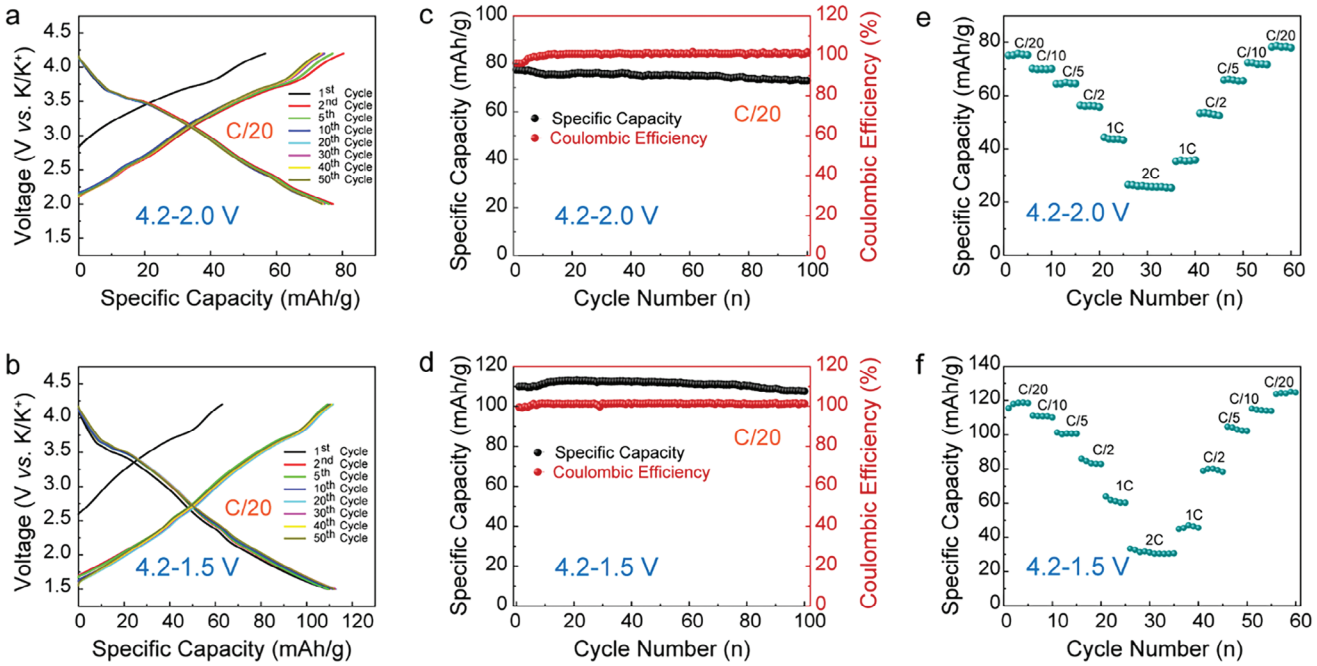

Figure 4. K^+ storage properties of KNM at room temperature (25 °C) across a potential window range of a, c, e) 4.2–2.0 V and b, d, f) 4.2–1.5 V. a, b) Galvanostatic (dis)charge profiles at a current rate of C/20, c, d) specific discharge capacity and Coulombic efficiency up to 100th cycles at a C/20 current rate and e, f) stability at different current rates. Here, 1C corresponds to the current rate of 124.37 mAg^{-1}.

KTFSA in Pyr_{13}TFSA ionic liquid electrolyte was employed. Without any cathode optimization, KNM delivered a reversible capacity of ≈113 mAh g^{-1} (≈0.45 moles of K^+) and ≈80 $mAhg^{-1}$ (≈0.32 moles of K^+) in the electrochemical potential windows of 4.2–1.5 and 4.2–2.0 V, respectively, with excellent cyclability over initial 50 cycles (**Figure** 4a,b). The higher initial discharge capacity over the charge capacity suggests a greater number of K^+ ions intercalate into the host structure. The galvanostatic voltage profiles suggest a multistep redox process with sloping voltage profiles and reversible K^+ (de)insertion at average voltages of 3.2 and 2.7 V, respectively, signifying a (topotactic) solid solution behavior upon (de)potassiation. Further, near-perfect capacity retention and Coulombic efficiency were observed at the end of 100 cycles in both potential windows, indicative of good structural integrity of the P3 layered oxide framework (Figure 4c,d). KNM exhibited moderate rate capability at different current rates at 25 °C (Figure 4e,f), which may be attributed to the slow K^+ migration due to the high viscosity of the KTFSA-based electrolyte.

Additionally, the potassium storage properties of the KNM host were tested at higher temperatures (i.e., 40 °C and 50 °C) in half-cell configurations inside a temperature-controlled chamber (**Figure** 5; Figure S11, Supporting Information). When cycled at 50 °C, KNM exhibited a reversible capacity of 106 and 140 mAh g^{-1}, corresponding to a reversible insertion of 0.43 and 0.56 mol of K^+ in the host framework, when lower cut off voltage was restricted to 2.0 and 1.5 V, respectively (Figure 5a,b). The capacity retention of 82% (79%) over 100 cycles along with Coulombic efficiency of 98% (90%) in the potential window of 4.2–2.0 (4.2–1.5) V further demonstrates excellent electrochemical reversibility of KNM cathode at a higher temperature as well (Figure 5c,d). Upon high-temperature cycling, excellent rate capability was observed in both voltage windows (Figure 5e,f) owing to the elevated K^+ ionic conductivity in the electrolyte at high temperatures. The electrochemical performance at 40 °C lies between the electrochemical activity observed at 25 °C and 50 °C, delivering an initial charge and discharge capacity of ≈87 mAh g^{-1} (0.35 mol of K^+), and ≈120 mAh g^{-1} (0.48 mol of K^+), respectively, for 4.2–2.0 V and 4.2–1.5 V windows. Notably, no significant change in the average redox potential was observed irrespective of testing temperature. Thus, KNM works as a stable K^+ insertion host with the potential to function at ambient as well as high-temperature conditions. Notably, we observe a comparable K^+ storage behavior of KNM host synthesized via the sol–gel method (Figure S12, Supporting Information). The slight increase in capacity can be attributed to smaller and more uniform particles.

Potentiostatic intermittent titration (PITT) experiments were conducted to investigate the K^+ (de)intercalation mechanism into the host structure by employing 10 mV increments with 1 h rest at each step with a scan rate of C/50 at 25 °C (Figure S13, Supporting Information). A Cottrell-type curve was observed throughout the cycle that signals a continuous solid–solution (or single-phase) redox mechanism during potassium insertion/removal.

2.4. Postmortem Analyses

To probe the underlying redox mechanism, ex situ synchrotron XRD patterns (Figure S14a, Supporting Information) were acquired at different (de)potassiation states during (dis)charge cycles: at the end of first charge (4.2 V), discharge up to 2.0 V and for the discharge up to 1.5 V. Gradual peak shift was

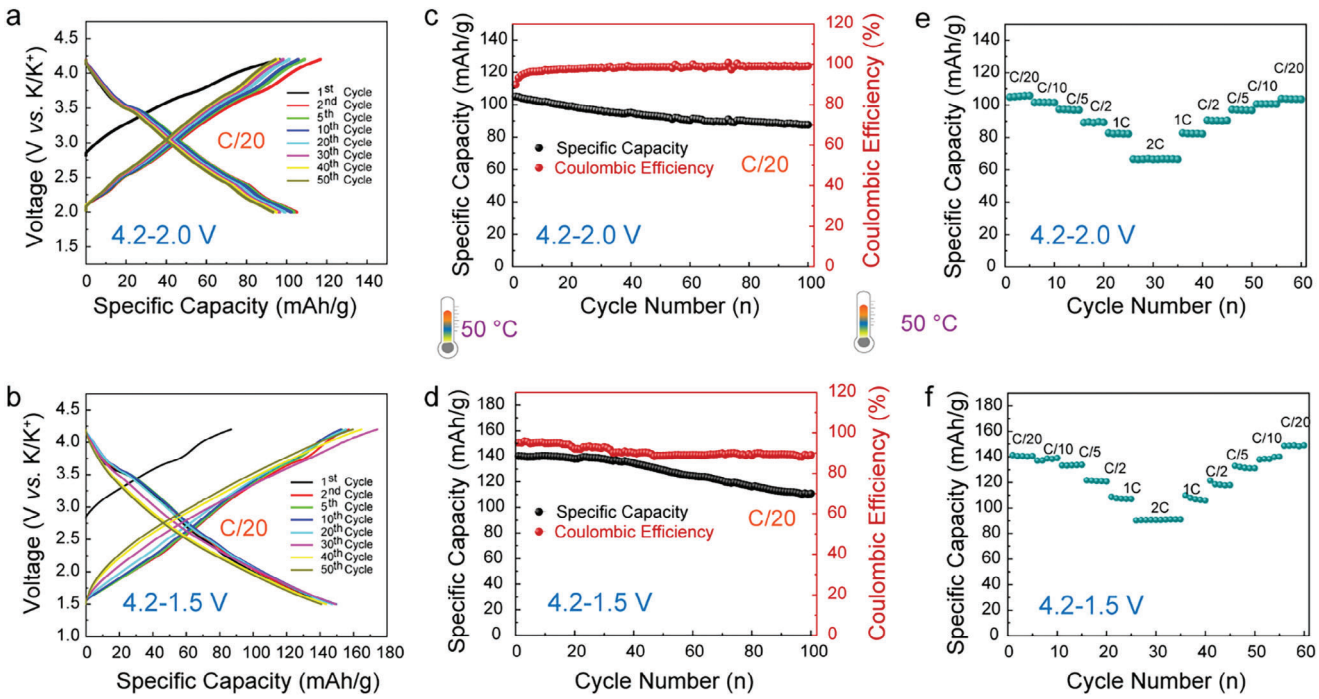

Figure 5. K^+ storage properties of KNM at elevated temperature (50 °C) across a potential window range of a, c, e) 4.2–2.0 V and b, d, f) 4.2–1.5 V. a, b) Galvanostatic (dis)charge profiles at a current rate of C/20, c, d) specific discharge capacity and Coulombic efficiency up to 100th cycles at a C/20 current rate and e, f) stability at different current rates.

observed during reversible K^+ (de)insertion, indicative of a solid solution (single-phase) redox mechanism. During (de)potassiation, a small change in *d*-spacing was observed due to the alteration in the bonding between O and Ni/Mn (due to changes in electron density in the vicinity of Ni/Mn during K^+ (de)insertion). However, a small change in the (003) peak position was observed corresponding to a minor alteration in the *c*-axis or the interlayer spacing between the adjacent MO_6 layers (Table S4, Supporting Information). Upon potassiation (discharging), the XRD peaks and *d*-spacing shifted back to the original values, indicating high structural reversibility. Thus, the PITT and ex situ XRD analysis confirmed the occurrence of a solid solution (de)potassiation redox mechanism.

Figure S14b (Supporting Information) shows the Raman spectra at various states of (dis)charge. The Raman bands for pristine and discharged samples were almost unaltered while these bands shifted upward for the charged (4.2 V) state. In the case of $LiCoO_2$, the opposite behavior (downward shift) is observed due to an increase in electrostatic repulsion between oxygen–oxygen contacts with the removal of the Li, which is also linked to the expansion along the *c*-axis. For KNM, the observed upward shift of the band could be due to the increase in covalent bonding between Ni and O, especially when Ni is in a 4+ state or a more localized electronic charge distribution within the MO_6 layers, as K is removed.[21] The upward shift is consistent with ex situ XRD, as there is a subtle shift in the position of the initial peak (003), indicating a lack of severe expansion along the *c*-axis. Notably, the broadening of Raman bands for the discharged state (at 1.5 V) could be due to the increase in distortion in the lattice at higher K content.

To probe the material at the atomic scale, TEM analysis was conducted at different states of (de)potassiation (**Figure 6**). Independent of the state of (dis)charge, the SAED patterns revealed diffraction spots corresponding to a rhombohedral crystal system, which concurs with the underlying solid solution reaction mechanism during (de)potassiation. The clear lattice fringes and the corresponding plane observed in the HRTEM images of all samples further signified the structural integrity of KNM. EDS mapping attested to the uniform distribution of constituent elements (Figure S15, Supporting Information). Notably, the superlattice spots present in the pristine material (Figure 1j) were still evident in both the fully charged (4.2 V) and discharged (2.0 V/1.5 V) cathode samples. These superlattice spots coexisted alongside the regular bright spots, emphasizing the persistence of in-plane Ni-Mn ordering, thus reducing the possibility of any transition metal (especially Mn) migration to K layers, resulting in a stable structure during cycling. Notably, the integrity of the P3-type structure and in-plane Ni–Mn remains unaltered in KNM with the battery cycling, indicating its robust K^+ storage capability (Figure S16 and S17, Supporting Information).

To analyze the oxidation states of Ni, Mn, and O in the pristine and (dis)charged KNM samples, ex situ XPS measurements were conducted. **Figure 7** shows the XPS spectra of the Ni 2*p* and Mn 2*p* core levels for the as-prepared KNM sample, after charging to 4.2 V, discharging to 2.0 V, and discharging to 1.5 V. The XPS analyses of Ni 2*p* and Mn 2*p* species are compiled in Table S5 (Supporting Information). Both Ni 2*p* and Mn 2*p* spectra consist of two prominent peaks, at binding energies of 854.2 and 871.5 eV for Ni, and at binding energies of ≈641 and ≈653.9 eV for Mn, which correspond to the $2p_{3/2}$ and $2p_{1/2}$ spin–orbit doublets, respectively, in both transition metals. The core-level

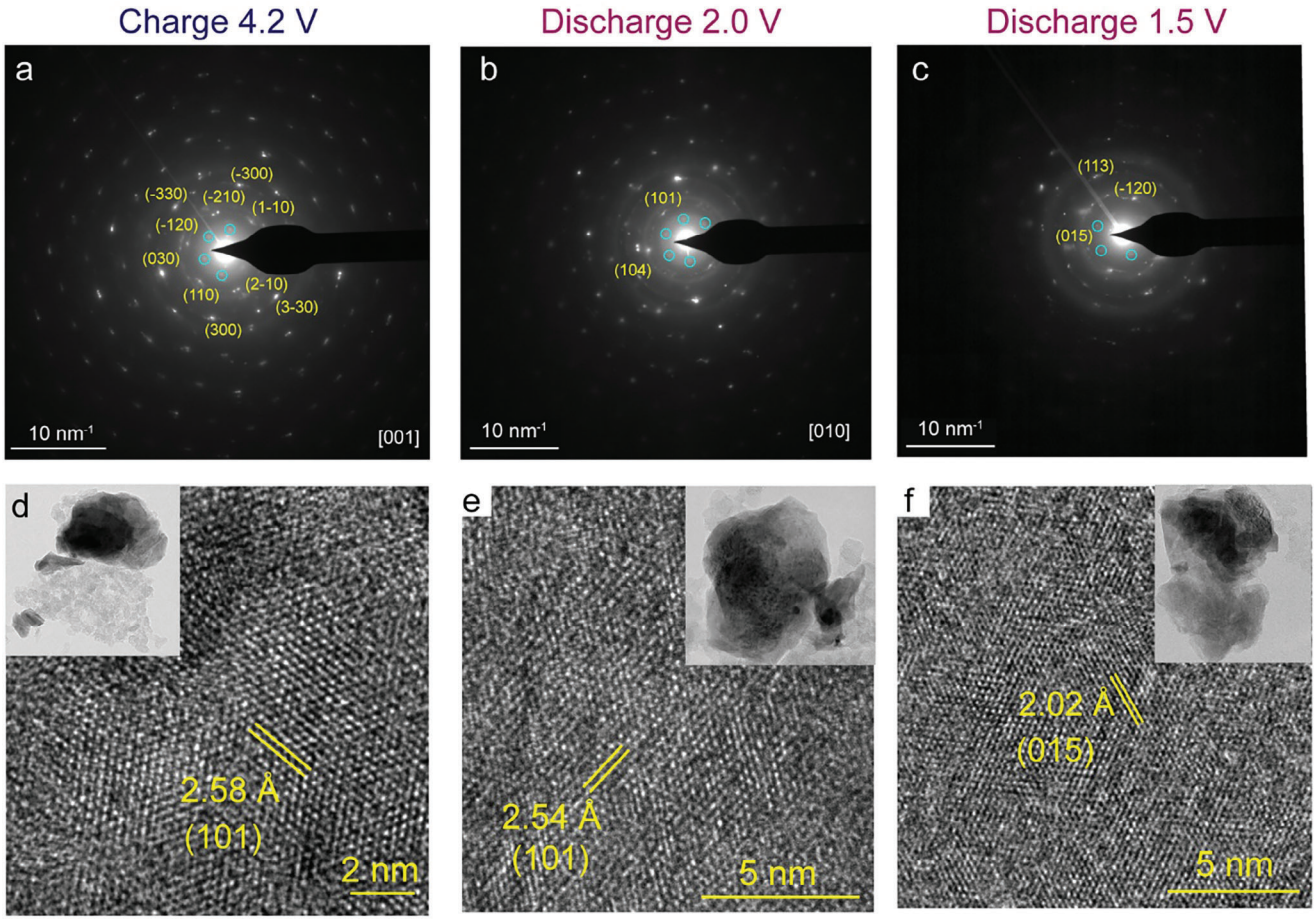

Figure 6. SAED patterns for KNM cathode at different states of (dis)charge: a) charged at 4.2 V, b) discharged to 2.0 V, and c) discharged to 1.5 V. In each case, superstructure peaks are highlighted by blue circles. d, e, f) Corresponding HRTEM images showing lattice fringes along with the TEM images (inset).

binding energies of Ni and Mn were investigated using the curve-fitting models proposed by Biesinger et al. and Nesbitt et al.[22] The oxidation state of Ni and Mn varies between 2+, 3+, and +4 depending on the different states of (de)potassiation. Notably, in pristine KNM, the broad envelope of Ni 2*p* core level spectrum indicates that the Ni is in multi-oxidation states (i.e., 2+ and 3+). Indeed, this spectrum can be fitted into sets of spin–orbit doublet along with associated satellite peaks, which can be assigned to Ni^{2+} and Ni^{3+} states. While the Mn 2*p* peak can be deconvoluted into two predominant peaks, each peak can be further deconvoluted into five peaks, mostly dominated by the 4+ oxidation state along with the presence of residual Mn^{3+} in the compound.

Upon charging to 4.2 V, the Ni 2*p* spectrum broadened and shifted to higher binding energies, indicating a change in oxidation state to Ni^{3+} and Ni^{4+}. The Mn 2*p* spectrum reflects the Mn^{4+} oxidation state as in the case of the pristine KNM. Upon discharging to 2.0 V, the Ni 2*p* and Mn 2*p* spectra shifted to lower binding energy, indicating a change in oxidation state to Ni^{2+} and Mn^{3+}, respectively. Upon further discharging to 1.5 V, Ni 2*p* spectra remained unaltered, while the changes in the Mn spectrum indicated a reduction of Mn^{3+} to Mn^{2+}, thus confirming that the low-voltage redox can be solely assigned to the Mn redox center.

The O 1*s* spectrum displayed the characteristics of the O^{2-} anions present in the crystalline framework. There was no evidence of formal $(O_2)^{n-}$ species or undercoordinated oxygen ions. The absence of any significant changes in the O 1*s* spectrum upon (dis)charging ruled out the possibility of any oxygen (anionic) redox processes. The small changes in the O 1*s* peak were possibly due to the deposited species at the electrode/electrolyte interface during cycling. The ex situ XPS results suggest that the redox process in KNM is reversible, and the net electrochemical (de)potassiation capacity arises solely from the transition metal redox.

3. Discussion

Herein, we have investigated the P3-type $K_{0.5}Ni_{1/3}Mn_{2/3}O_2$ framework as a potential cathode material for KIBs using a combination of experimental and computational methods. Our results suggest that KNM is a promising cathode material for KIBs exhibiting high capacity and good cycling stability. Specifically, we observed the KNM cathode offers robust performance both at ambient as well as high temperatures, making it suitable for applications ranging from small-scale tools to stationary storage. We find a solid–solution phase behavior during K^+

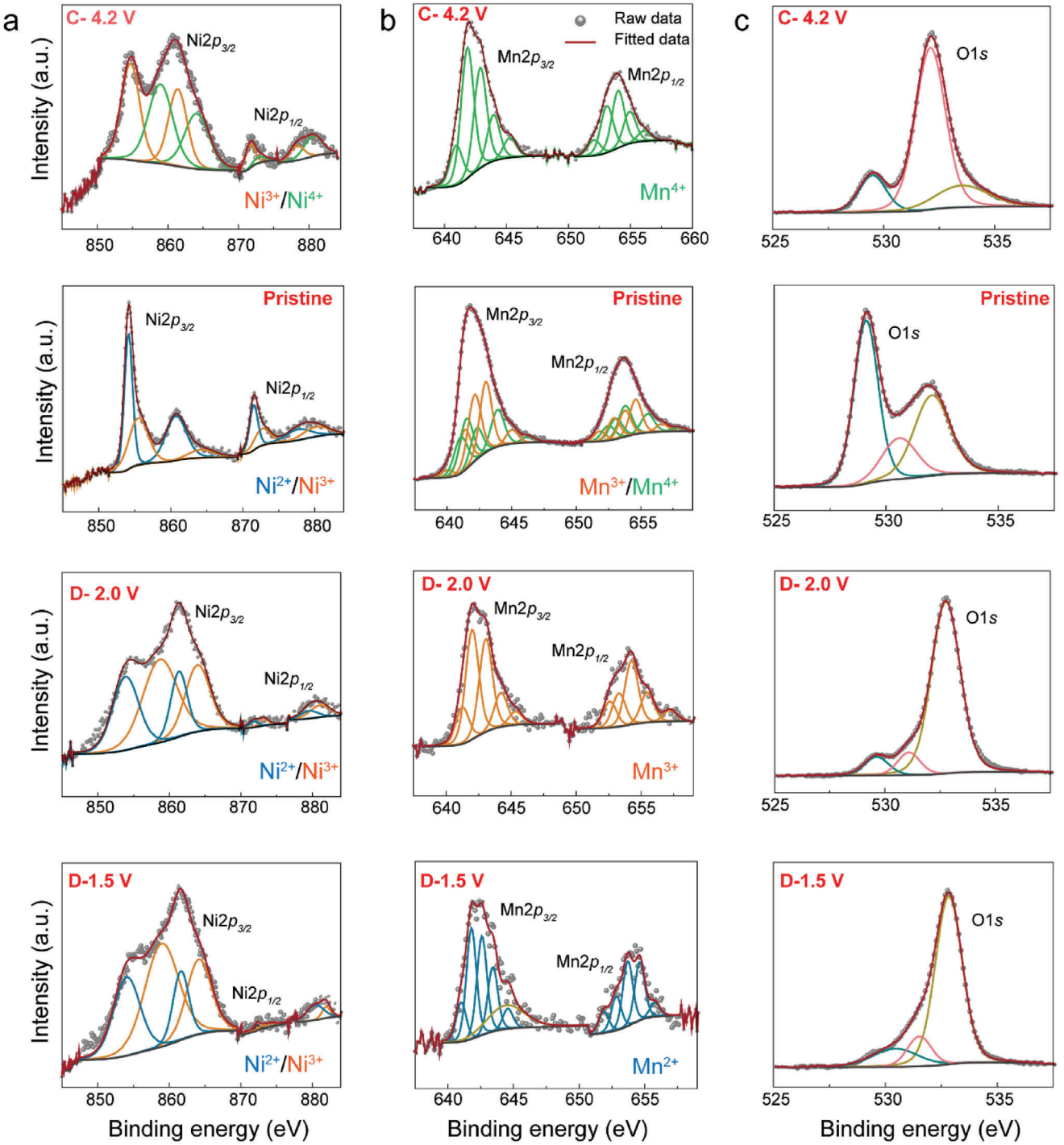

Figure 7. High-resolution XPS spectra for KNM probing a) Ni 2*p*, b) Mn 2*p*, and c) O 1*s*. The rows indicate different states of (de)potassiation, namely charged (at 4.2 V, top row), pristine KNM (second row from top), discharged (at 2.0 V, third row from top), and discharged (at 1.5 V, bottom row). The shifting of the Ni and Mn peaks toward higher (lower) binding energy at the charged (discharged) states confirms the change in the redox state of Ni and Mn. The set of peaks with blue, orange, and green corresponds to 2+, 3+, and 4+ oxidation states respectively in the case of Ni and Mn. D and C labels within each panel indicate the discharged and charged state.

(de)intercalation with structural reversibility. The KNM cathode involves the ordering of Ni and Mn in the transition metal layers, which is largely affected by the K content in the P3 system. Finally, we observe that the redox behavior of KNM upon (de)potassiation arises entirely from the transition metal redox centers, with Mn and Ni contributing to the low and high voltage regions, respectively.

The galvanostatic (dis)charge profiles for KNM are "smoother" than those of $K_{0.5}MnO_2$,[10] revealing the lack of any complex phase transformations during K^+ removal/insertion, including at higher temperatures. Further, we did not find any significant change in the average K-insertion voltage as a function of temperature, indicating the stable electrochemical activity of KNM. We observe superior rate kinetics at higher temperatures in KNM, owing to the enhanced ionic conductivity in the electrolyte as well as the host structure. Notably, lower Columbic efficiency at higher temperatures indicates the possibility of O_2 evolution at a higher voltage. Oxygen anions 2*p* orbital is strongly hybridized to Ni-3*d* orbitals, which takes it to a higher energy state along with the Ni-3*d* states. It could be possible that temperature provides the additional energy for oxygen to escape from the lattice, which is not possible at room temperature. We are currently investigating the possible O_2 evolution at a higher temperature, which will be reported in the future. The galvanostatic tests, cyclic voltammetry, and XPS data suggest the capacity of KNM is derived from two different sources: Ni redox at higher voltage region (4.2–3.0 V; $Ni^{3+/4+} \rightarrow Ni^{2+/3+}$) and Mn redox at lower voltage region (3.0–1.5 V; $Mn^{4+} \rightarrow Mn^{2+/3+}$). Below 2.0 V, Mn changes its redox state from 3+ to 2+ during K^+ insertion leading to extra capacity across the wider electrochemical window.

Experimentally observed lower (≈ 0.3 V) average voltage in KNM with respect to similar Na counterparts can be correlated with the bonding nature of transition metal and oxygen ions.[23] This can be attributed to the strong electrostatic interaction of the large K^+–K^+ ions in the K-layer, leading to higher M–O bond length (weak covalent bonding) than Na-based layered materials.[24] Further, the overestimation of voltage by DFT, compared to our experiments, could be the result of underestimating the energy of the depotassiated state ($Ni_{1/3}Mn_{2/3}O_2$) as well as the fact that the range of K concentrations accessed experimentally is different from the range used in calculations. Typically, the fully charged phases are thermodynamically metastable, and DFT, specifically SCAN+*U*, underestimates the energies of metastable and unstable phases, leading to an overestimated voltage.[20a] Similarly, all the exchange-correlation (XC) functionals considered in this study underestimate the interaction between the large inter-slab spacings caused by the large K^+ ions. This leads to a lower (8–10%) calculation of the lattice parameter in the *c*-direction.

The DFT (SCAN+*U*) calculation further reveals the in-plane Ni–Mn cation ordering MO_2 sheets, which depend on the K-content in the framework. The in-plane transition metal ordering results from two different charged ions with variable ionic sizes present in the lattice. Owing to the distinct oxidation states on transition metals, the electrostatic interaction between the cations can be different. As a result, the lattice would try to arrange the charged species in such a way that the electrostatic repulsion and complicated orbital interaction between large K^+ ions and the transition metal ions could be minimized. Notably, the close relationship between the K content in the framework and the Mn–Ni superstructure in MO_2 sheets points to the fact that electrostatic interaction is a dominating factor in deciding the superlattice structure. In addition, the stacking of the $\sqrt{3}a \times \sqrt{3}a$ superstructure ordered MO_2 sheets requires larger unit cells. The large hexagonal cell with an axis, A_{hex}, $\sqrt{3}$ times larger than that of the small hexagonal unit cell, $A_{hex} = 2.90$, is the natural unit cell of the $\sqrt{3}a \times \sqrt{3}a$ superstructure. As per DFT prediction, superstructure spots were identified by electron microscopy. One can expect (1/3,1/3, n) extra peaks in the XRD and TEM SAED pattern.

4. Conclusion

In summary, we have investigated the P3-type $K_{0.5}Ni_{1/3}Mn_{2/3}O_2$ (KNM) layered oxide as a promising cathode insertion material for potassium-ion batteries. The structural, morphological, electronic, and ground state in-plane transition metal ordering, as well as its electrochemical properties at room and elevated temperatures, have been explored synergizing experimental and theoretical methods. Involving both Ni^{4+}/Ni^{3+} and $Mn^{4+}/Mn^{3+}/Mn^{2+}$ redox processes, KNM offers an average working potential centered ≈3.2 V (vs K/K^+) and discharge capacity exceeding 100 mAh g^{-1}. KNM undergoes a topotactic solid solution reaction offering robust structural/cycling stability and rate kinetics. The electrochemical performance was found to be stable even at high temperatures (40–50 °C). We observed that partial substitution of Ni for Mn can not only increase the electronic conductivity of KNM, but can also mitigate the complex phase transformation occurring at higher voltages in the pure Mn-based host. Our computational studies have also revealed that the Ni–Mn preferential configurations in the transition metal layers are strongly correlated with K-content in the KNM structure. Overall, this work introduces P3-type $K_{0.5}Ni_{1/3}Mn_{2/3}O_2$ as a new cathode material for potassium-ion batteries, broadens the oxide material database for KIBs, and offers new impetus to develop other binary metal oxides for superior potassium storage systems.

5. Experimental Section

Material Synthesis: The targeted P3-type $K_{0.5}Ni_{1/3}Mn_{2/3}O_2$ layered oxide was synthesized by solid-state synthesis using stoichiometric amounts of K_2CO_3 (SDFCL, 99%), MnO_2 (Sigma–Aldrich, 95%), and NiO (SDFCL, 99%) (in molar ratio K: Mn: Ni = 0.5: 0.67: 0.33). 10 wt.% excess K_2CO_3 was added to compensate for the inevitable K evaporation during calcination. The precursors were intimately mixed by planetary ball milling for 6 h at 350 rpm in acetone media. This homogeneous precursor mixture was further grounded by mortar and pestle and was pelletized by applying uniaxial hydraulic pressure (10 MPa). These pellets were calcined at 800 °C for 24 h in air and were cooled to ambient temperature. The annealed product was transferred to an argon-filled glove box to avoid moisture contamination. Alternately, P3-type $K_{0.5}Ni_{1/3}Mn_{2/3}O_2$ was prepared via sol–gel route using $(CH_3COO)_2Mn.4H_2O$ (ThermoFisher Scientific, 99%), $(CH_3COO)_2Ni.4H_2O$ (SDFCL, 99%), $(CH_3COO)K$ (SDFCL, 99%) and citric acid (SDFCL, 99.5%) precursors. First, the K-acetate, Mn-acetate, and Ni-acetate were dissolved in distilled water in the molar ratio of 3:4:2 (under steady magnetic stirring). Following, citric acid (chelating agent) was added to the solution dropwise, which led to the formation of the gel. The resulting gel was dried at 100 °C in air to obtain the dried gel

precursor. Finally, the dried gel precursor was heated at 800 °C for 12 h to yield the desired product.

Structural and Physical Characterizations: The crystal structure was determined by X-ray diffraction (XRD) using a PANalytical X'pert pro diffractometer equipped with Cu K_α (λ_1 = 1.5405 Å, λ_2 = 1.5443 Å) radiation source operating at 40 kV/30 mA, with Ni-filter acting as a monochromator. Rietveld refinement was performed using FullProf suites, and the crystal structures were illustrated using the VESTA-3 software.[25] The morphology of as-prepared active materials was examined with a Carl Zeiss Ultra55 field emission scanning electron microscope (FESEM) unit with a thermal field emission-type tungsten source operating in the range of 0.1–20 kV. The spatial elemental distribution was further observed using an energy-selective backscattered (ESB) detector at 15 kV in both line and area scan modes. An FEI Tecnai F20 S-twin TEM unit was used to record the selected area electron diffraction (SAED) patterns, high-resolution transmission electron microscopy (HRTEM), and bright-field images.

Electrochemical Measurements: The working electrode (thin sheet) was prepared inside an argon-filled glove box from the mixture of 75% KNM powder (active material), 15% carbon black, and 10% teflonized acetylene black (c-TAB) binder using mortar and pestle. The sheet was then cut into a disc shape of 12 mm diameter with an active material load of about ≈ 4–5 mg. The electrochemical behavior of the as-prepared working electrodes was studied by CR2032 coin-type half-cells assembled inside an argon-filled glovebox (MBraun LabStar GmbH, O_2 and H_2O < 0.5 ppm) against potassium metal as a counter electrode and reference electrode. The electrodes were separated by a glass fiber separator (Whatman, GF/C) soaked in 0.5 M KTFSI (bis(trifluoromethanesulfonyl) imide) salt in Pyr_{13}TFSI in (1-methyl-1-propylpyrrolidinium bis(trifluoromethanesulfonyl) amide) acting as electrolyte.[26] All electrochemical testing was performed using the Neware BTS-4000 battery tester in two potential windows (1.5–4.2 V and 2–4.2 V) at various rates (C/20 to 2C) and different temperatures (25–50 °C).

Postmortem Analyses: Ex situ analyses were performed after disassembling cycled Swageloks inside the glove box. The recovered electrodes were washed with dimethyl carbonate (DMC, anhydrous, 99%), and were dried overnight. These electrodes were subjected to X-ray analysis (XRD and XPS). XPS spectra were recorded using a Thermo-Scientific K-XPS device operating at 12 kV/6 mA.

Computational Methods: Vienna ab initio Simulation Package (VASP) was employed to perform all spin-polarizated DFT calculations using projected augmented wave (PAW) potentials.[27] The plane-wave basis sets were expanded up to a kinetic energy cutoff of 520 eV and a dense, Γ-centered Monkhorst-Pack *k*-mesh with a minimum density of 48 subdivisions along each reciprocal lattice vector was used to sample the Brillouin zone, with a Gaussian smearing (of width 0.05 eV) used to integrate the Fermi surface.[28] The structure relaxation was performed using the conjugate gradient scheme with an atomic force convergence criterion of |0.01| eV $Å^{-1}$ and a total energy convergence criterion of 10^{-6} eV. The magnetic moments of Ni and Mn were initialized in low-spin and high-spin ferromagnetic ordering respectively.[29] The cell volume, shape, and positions of all ions were relaxed for all structures without preserving any symmetry. The SCAN exchange–correlation functional was deployed as it estimates better relative phase stability, electronic properties, and diffusivity than the conventional PBE (+*U*) approach.[30] In addition, effective Hubbard *U* parameters of 2.5 and 2.7 eV for Ni and Mn, respectively, mitigate the fictitious self-interactions among 3*d* electrons of transition metals, in the case of SCAN+*U*.[32] The *U* values utilized in GGA+*U* calculations were 3.9, and 6.2 eV for Mn, and Ni, respectively.[31] The pymatgen tool was utilized to enumerate all symmetrically unique orderings since the KNM structure can take on a variety of K-vacancy and Ni–Mn configurations.[32] Further, among various ordered structures, the ordered structure with the lowest energy derived by the considered DFT framework was used for further calculations and analyses.

A reversible K^+ (de)intercalation into the P3-type KNM host structure can be represented by the following redox reaction:

$$zK^+ + ze^- + K_{0.5-z}Ni_{1/3}Mn_{2/3}O_2 \rightarrow K_{0.5}Ni_{1/3}Mn_{2/3}O_2 \quad (1)$$

The topotactic intercalation average voltage can be calculated from Gibbs free energy change, which can be further approximated by the total ground state energy change as calculated by DFT ($\Delta G \approx \Delta E$),[33] ignoring the *p*–V and entropic contributions energies at room temperature as:

$$V = -\frac{\left(E_{K_{0.5}Ni_{1/3}Mn_{2/3}O_2} - E_{K_{0.5-x}Ni_{1/3}Mn_{2/3}O_2} - xE_K\right)}{xF} \quad (2)$$

where $E_{K_{0.5}Ni_{1/3}Mn_{2/3}O_2}$ is DFT calculated energy of the most stable state configuration of $K_{0.5}Ni_{1/3}Mn_{2/3}O_2$, $E_{K_{0.5-x}Ni_{1/3}Mn_{2/3}O_2}$ is the energy of depotassiated state and E_K represents the energy of ground state bcc K metal (*Im-3m* space group).

Supporting Information

Supporting Information is available from the Wiley Online Library or from the author.

Acknowledgements

The current work was financially supported by the Department of Science and Technology (Government of India) under the Core Research Grant (CRG/2022/000963). P.K.J. and K.S. are grateful to the Ministry of Human Resource Development (MHRD, Government of India) for financial assistance. G.S.G. acknowledges financial support from the Science and Engineering Research Board (SERB) of the Government of India, under sanction numbers SRG/2021/000201 and IPA/2021/000007. P.K.J. and G.S.G. acknowledge the computational resources provided by the Supercomputer Education and Research Centre (SERC), IISc. Microscopy analyses was performed using the facilities at the Micro-Nano Characterization Facility (MNCF, CeNSe, IISc) and the Advanced Facility for Microscopy and Microanalysis (AFMM, IISc). P.B. is grateful to the Alexander von Humboldt Foundation (Bonn, Germany) for a 2022 Humboldt fellowship for experienced researchers. Microscopy part of this work was performed using the facilities at the micro-nano characterization facility (MNCF), CeNSE, IISc, and advanced center for microscopy and microanalysis (AFMM), IISc. This work contributes to the research performed at CELEST (Center for Electrochemical Energy Storage Ulm-Karlsruhe).

Conflict of Interest

The authors declare no conflict of interest.

Data Availability Statement

The data that support the findings of this study are available in the supplementary material of this article.

Keywords

cathodes, energy storage, P3-type layered oxides, potassium-ion batteries

Received: March 20, 2024
Revised: May 8, 2024
Published online: May 22, 2024

[1] a) M. Armand, J. M. Tarascon, *Nature* **2008**, *451*, 652; b) M. S. Whittingham, *Chem. Rev.* **2014**, *114*, 11414; c) B. Dunn, H. Kamath, J.-M. Tarascon, *Science* **2011**, *334*, 928.

[2] a) T. Hosaka, K. Kubota, A. S. Hameed, S. Komaba, *Chem. Rev.* **2020**, *120*, 6358; b) H. Kim, J. C. Kim, M. Bianchini, D.-H. Seo, J. Rodriguez-Garcia, G. Ceder, *Adv. Energy Mater.* **2018**, *8*, 1702384.
[3] a) Y. Matsuda, H. Nakashima, M. Morita, Y. Takasu, *J. Electrochem. Soc.* **1981**, *128*, 2552; b) M. Okoshi, Y. Yamada, S. Komaba, A. Yamada, H. Nakai, *J. Electrochem. Soc.* **2017**, *164*, A54; c) J.-Y. Hwang, S.-T. Myung, Y.-K. Sun, *Adv. Funct. Mater.* **2018**, *28*, 1802938.
[4] R. Shannon, *Acta Cryst* **1976**, *32*, 751.
[5] a) P. K. Jha, V. Pralong, M. Fichtner, P. Barpanda, *Curr. Opin. Electrochem.* **2023**, *38*, 101216; b) X. Zhang, Z. Wei, K. N. Dinh, N. Chen, G. Chen, F. Du, Q. Yan, *Small* **2020**, *16*, 2002700.
[6] a) P. K. Jha, S. N. Totade, P. Barpanda, G. Sai Gautam, *Inorg. Chem.* **2023**, *62*, 14971; b) C. Zhao, Q. Wang, Z. Yao, J. Wang, B. Sánchez-Lengeling, F. Ding, X. Qi, Y. Lu, X. Bai, B. Li, H. Li, A. Aspuru-Guzik, X. Huang, C. Delmas, M. Wagemaker, L. Chen, Y. S. Hu, *Science* **2020**, *370*, 708.
[7] H. Kim, D.-H. Seo, A. Urban, J. Lee, D.-H. Kwon, S.-H. Bo, T. Shi, J. K. Papp, B. D. McCloskey, G. Ceder, *Chem. Mater.* **2018**, *30*, 6532.
[8] a) M. M. Claude Delmas, C. Fouassier, P. Hagenmuller, *Mater. Res. Bull.* **1976**, *11*, 1483; b) C. Delmas, C. Fouassier, P. Hagenmuller, *Physica B+C* **1980**, *99*, 81; c) C. Fouassier, C. Delmas, P. Hagenmuller, *Mater. Res. Bull.* **1975**, *10*, 443; d) M. D. Radin, A. Van der Ven, *Chem. Mater.* **2016**, *28*, 7898.
[9] a) K. Kubota, S. Kumakura, Y. Yoda, K. Kuroki, S. Komaba, *Adv. Energy Mater.* **2018**, *8*, 1703415; b) R. J. Clément, P. G. Bruce, C. P. Grey, *J. Electrochem. Soc.* **2015**, *162*, A2589.
[10] H. Kim, D.-H. Seo, J. C. Kim, S.-H. Bo, L. Liu, T. Shi, G. Ceder, *Adv. Mater.* **2017**, *29*, 1702480.
[11] a) X. Wang, X. Xu, C. Niu, J. Meng, M. Huang, X. Liu, Z. Liu, L. Mai, *Nano Lett* **2017**, *17*, 544; b) Z. Xiao, F. Xia, L. Xu, X. Wang, J. Meng, H. Wang, X. Zhang, L. Geng, J. Wu, L. Mai, *Adv. Funct. Mater.* **2022**, *32*, 2108244; c) P. K. Jha, P. Barpanda, *Inorg. Chem.* **2024**, *63*, 7137.
[12] a) Z. Xiao, J. Meng, F. Xia, J. Wu, F. Liu, X. Zhang, L. Xu, X. Lin, L. Mai, *Energy Environ. Sci.* **2020**, *13*, 3129; b) C. Liu, S. Luo, H. Huang, Z. Wang, A. Hao, Y. Zhai, Z. Wang, *Electrochem. commun.* **2017**, *82*, 150; c) L. Liu, J. Liang, W. Wang, C. Han, Q. Xia, X. Ke, J. Liu, Q. Gu, Z. Shi, S. Chou, S. Dou, W. Li, *ACS Appl. Mater. Interfaces* **2021**, *13*, 28369.
[13] a) P. Hohenberg, W. Kohn, *Phys. Rev.* **1964**, *136*, B864; b) W. Kohn, L. J. Sham, *Phys. Rev.* **1965**, *140*, A1133.
[14] a) J. M. Paulsen, J. R. Dahn, *Solid State Ion.* **1999**, *126*, 3; b) J. M. Paulsen, R. A. Donaberger, J. R. Dahn, *Chem. Mater.* **2000**, *12*, 2257.
[15] K. Sada, P. Barpanda, *Chem. Commun.* **2020**, *56*, 2272.
[16] T. Itoh, H. Sato, T. Nishina, T. Matue, I. Uchida, *J. Power Sources* **1997**, *68*, 333.
[17] a) J. Sun, A. Ruzsinszky, J. P. Perdew, *Phys. Rev. Lett.* **2015**, *115*, 036402; b) J. P. Perdew, K. Burke, M. Ernzerhof, *Phys. Rev. Lett.* **1996**, *77*, 3865; c) S. L. Dudarev, G. A. Botton, S. Y. Savrasov, C. J. Humphreys, A. P. Sutton, *Phys. Rev. B* **1998**, *57*, 1505; d) V. I. Anisimov, J. Zaanen, O. K. Andersen, *Phys. Rev. B* **1991**, *44*, 943; e) O. Y. Long, G. Sai Gautam, E. A. Carter, *Phys. Rev. Mater.* **2020**, *4*, 045401; f) G. Sai Gautam, E. A. Carter, *Phys. Rev. Mater.* **2018**, *2*, 095401.
[18] a) O. A. Vydrov, T. Van Voorhis, *J. Chem. Phys.* **2010**, 133; b) R. Sabatini, T. Gorni, S. de Gironcoli, *Phys. Rev. B* **2013**, *87*, 041108.
[19] S. Grimme, J. Antony, S. Ehrlich, H. Krieg, *J. Chem. Phys.* **2010**, *132*, 154104.
[20] a) O. Y. Long, G. Sai Gautam, E. A. Carter, *Phys. Chem. Chem. Phys.* **2021**, *23*, 24726; b) P. K. Jha, S. Singh, M. Shrivastava, P. Barpanda, G. Sai Gautam, *Phys. Chem. Chem. Phys.* **2022**, *24*, 22756.
[21] D.-H. Seo, A. Urban, G. Ceder, *Phys. Rev. B* **2015**, *92*, 115118.
[22] a) H. W. Nesbitt, D. Banerjee, *Am. Mineral.* **1998**, *83*, 305; b) M. C. Biesinger, B. P. Payne, A. P. Grosvenor, L. W. M. Lau, A. R. Gerson, R. S. C. Smart, *Appl. Surf. Sci.* **2011**, *257*, 2717.
[23] L. Yang, Y. Sun, P. Adelhelm, *Energy Technol* **2022**, *10*, 2101121.
[24] J. B. Goodenough, K. Mizushima, T. Takeda, *Jpn. J. Appl. Phys.* **1980**, *19*, 305.
[25] a) J. Rodríguez-Carvajal, *Physica B* **1993**, *192*, 55; b) K. Momma, F. Izumi, *J. Appl. Cryst.* **2011**, *44*, 1272.
[26] K. Yoshii, T. Masese, M. Kato, K. Kubota, H. Senoh, M. Shikano, *ChemElectroChem* **2019**, *6*, 3901.
[27] a) G. Kresse, D. Joubert, *Phys. Rev. B* **1999**, *59*, 1758; b) G. Kresse, J. Furthmüller, *Phys. Rev. B* **1996**, *54*, 11169; c) G. Kresse, J. Hafner, *Phys. Rev. B* **1993**, *47*, 558.
[28] H. J. Monkhorst, J. D. Pack, *Phys. Rev. B* **1976**, *13*, 5188.
[29] K. M. Ho, C. L. Fu, B. N. Harmon, W. Weber, D. R. Hamann, *Phys. Rev. Lett.* **1982**, *49*, 673.
[30] R. Devi, B. Singh, P. Canepa, G. Sai Gautam, *npj Comput. Mater.* **2022**, *8*, 160.
[31] A. Jain, S. P. Ong, G. Hautier, W. Chen, W. D. Richards, S. Dacek, S. Cholia, D. Gunter, D. Skinner, G. Ceder, K. A. Persson, *APL Mater* **2013**, *1*, 011002.
[32] S. P. Ong, W. D. Richards, A. Jain, G. Hautier, M. Kocher, S. Cholia, D. Gunter, V. L. Chevrier, K. A. Persson, G. Ceder, *Comput. Mater. Sci.* **2013**, *68*, 314.
[33] a) M. K. Aydinol, A. F. Kohan, G. Ceder, K. Cho, J. Joannopoulos, *Phys. Rev. B* **1997**, *56*, 1354; b) M. K. Aydinol, A. F. Kohan, G. Ceder, *J. Power Sources* **1997**, *68*, 664.